doi:10.26443/seismica.v5i1.1845

Submarine seismicity monitoring with distributed acoustic sensing near Santorini and Kolumbo Volcano

Sara Klaasen [1,*], **Thomas Hudson** [1], **Sanchit Sachdeva**[1], **Paraskevi Nomikou** [2], **Andreas Fichtner** [1]

[1]Department of Earth and Planetary Sciences, ETH Zürich, Zürich, Switzerland, [2]Department of Geology and Geoenvironment, National and Kapodistrian University of Athens, Athens, Greece

Author contributions: *Conceptualization*: Sara Klaasen, Andreas Fichtner, Paraskevi Nomikou. *Formal Analysis*: Sara Klaasen, Sanchit Sachdeva. *Investigation*: Sara Klaasen, Paraskevi Nomikou, Andreas Fichtner. *Writing - Original draft*: Sara Klaasen. *Writing - Review & Editing*: Sara Klaasen, Thomas Hudson, Andreas Fichtner. *Supervision*: Thomas Hudson, Andreas Fichtner. *Funding acquisition*: Andreas Fichtner.

Abstract Submarine volcanoes and faults pose hazards to nearby populated islands, yet their inaccessibility limits monitoring efforts. The Christiana-Santorini-Kolumbo volcanic field is capable of generating devastating eruptions, earthquakes and tsunamis. The 2025 earthquake swarm near Kolumbo, causing the evacuation of thousands from their homes, underlines the need for accurate and real-time monitoring. We interrogate a 45 km dark fibre that extended from Santorini past the submarine volcano Kolumbo for two months in 2021, comparing the performance of the fibre with the existing monitoring network for earthquake detection and location. The detected quakes originated all over Greece, coming from any azimuth. We can reliably identify events, doubling the number of detections in the vicinity of the fibre and Kolumbo. For event location, the azimuthal coverage of the existing seismometer network outperforms the fibre, emphasising the importance of a nonlinear fibre layout. Our findings suggest that while the higher detection sensitivity of DAS leads to an information gain, the data analysis remains challenging. The data quality may be insufficient for automated workflows. The need for human input limits the potential of DAS for real-time monitoring, although the enhanced detection sensitivity in remote areas justifies the continued research of DAS for submarine volcano monitoring.

Production Editor: Andreas Llenos
Handling Editor: Lise Retailleau
Copy & Layout Editor: Oliver Lamb

Received: July 11, 2025
Accepted: December 2, 2025
Published: January 16, 2026

1 Introduction

Submarine hazards, such as earthquakes, landslides and volcanoes, pose risks to coastal populations, and early-warning systems may prevent the loss of human life. Off-shore industries, such as carbon capture and storage sites, oil rigs and wind farms, require constant monitoring to ensure profitable and safe operations. While ocean-bottom seismometers can record the seismic activity of these sites, their deployment and maintenance are expensive and laborious, and they are often unable to analyse data in real time.

Distributed acoustic sensing (DAS) is an emerging technology that may fill a gap as a continuous real-time submarine monitoring tool with a dense spatial network. DAS samples the wavefield along a fibre-optic cable that can extend up to a hundred kilometres, with a spatial resolution down to the sub-metre scale, and a broadband response with sampling rates up to the kHz range (e.g., Mateeva et al., 2014; Hartog, 2017; Lindsey and Martin, 2021; Jousset et al., 2018; Paitz et al., 2021). The ability of DAS to sample "dark" fibres, namely telecommunication fibres that are not in use, is especially beneficial in the submarine environment. Existing fibre-optic networks between islands or off-shore industries have the potential to transform into large seismic networks at no additional cost.

*Corresponding author: sara.klaasen@eaps.ethz.ch

DAS has been applied in a wide range of environments to monitor earthquakes (e.g., Wang et al., 2018; Li and Zhan, 2018; Nayak et al., 2021; Li et al., 2023; Gou et al., 2025), landslides (e.g., Xie et al., 2024; Ouellet et al., 2024), volcanoes (e.g., Klaasen et al., 2021; Nishimura et al., 2021; Currenti et al., 2021; Jousset et al., 2022; Biagioli et al., 2024), geothermal experiments (e.g., Lellouch et al., 2020; Azzola et al., 2023; Cheng et al., 2023; Martuganova et al., 2022; Tuinstra et al., 2024), wind farms (e.g., Trafford et al., 2022) and carbon capture and storage sites (e.g., Grandi et al., 2017; Joe et al., 2020; Pevzner et al., 2021). Submarine applications show that DAS is able to detect microseisms and teleseisms with dark fibres and characterise the subsurface (e.g., Williams et al., 2019; Spica et al., 2020; Lior et al., 2021; Cheng et al., 2021).

This experiment uses a dark fibre to monitor the submarine volcano Kolumbo in Greece. Kolumbo is part of the Christiana-Santorini-Kolumbo volcanic field and is currently the most active and hazardous submarine volcano in the Aegean Sea (Nomikou et al., 2019). An eruption in 1650 caused the death of 70 people and thousands of animals on the nearby island of Santorini, due to the tsunami and toxic gas release (Cantner et al., 2014; Ulvrova et al., 2016). The region is seismically active and generated the largest earthquake in Greece in 1956 (Ms 7.5) (Okal et al., 2009; Brüstle et al., 2014). Its most recent period of seismic unrest in 2025 with ∼200 earth-

quakes over M4.0 led to the evacuation of thousands of residents from Santorini. Continuous monitoring is necessary to mitigate the devastating impacts of volcanic eruptions and earthquakes on densely populated islands.

This work assesses the potential and challenges of DAS as a submarine monitoring tool, by examining its ability to detect and locate seismicity compared to the existing earthquake catalogue from the National Observatory of Athens (NOA) (Evangelidis and Melis, 2012), which is created with seismic stations located throughout the mainland and islands of Greece (e.g., University of Athens, 2008; Technological Educational Institute of Crete, 2006; (ITSAK) Institute of Engineering Seimology Earthquake Engineering, 1981; Aristotle University of Thessaloniki, 1981). In order to complement existing monitoring networks, the combination of DAS and seismometers needs to locally lower the detection threshold and accurately locate the seismicity. We detect seismic events using an image-processing algorithm and we locate them with travel times. We detect earthquakes throughout Greece, which arrive at the fibre coming from any azimuth. DAS seems to have a consistent detection threshold given the distance and magnitude of events, although this threshold is lowered for seismic clusters in line with the fibre. Additionally, we detect hundreds of events that the existing network misses, and we hypothesise that these events originate in the vicinity of Kolumbo and the fibre. However, even though the spatial density of DAS data has advantages for earthquake detection, the data quality of DAS can make travel time picking, phase identification and further analysis challenging. In the end, we manually pick the first arrivals for a selection of events, as the data is too incoherent for automated algorithms. Additionally, the spatial coverage of the existing network outperforms the spatial density of DAS for event location. This implies that while fibre-optic networks can lower the detection threshold, the earthquake analysis can be challenging and requires significant manual input. Even so, fibre-optic networks with a larger azimuthal coverage can contribute to targeted monitoring, as long as the data quality is carefully controlled and manual effort might need to be incorporated in the data analysis.

2 Experiment & Data

We interrogated a 45 km long fibre-optic cable that extends from the island of Santorini, to the island of Ios between 18 October 2021 and 15 December in 2021. Figure 1a shows the fibre layout with respect to the islands of Santorini and Ios, and the submarine volcano Kolumbo. The first 11 km of fibre follow the roads on Santorini, where we could use tap tests to geolocate the data. The fibre then extends into the Aegean Sea, where we have unknown cable coupling conditions and no exact locations for the fibre. The fibre ends at Ios. Unfortunately, the data quality at the end of the fibre was too low for tap tests. This means that we get location uncertainties on the order of 100 m for the submarine section of the fibre.

We used a Silixa iDAS v2 interrogator to sample the seismic wavefield every 8 m along the fibre with a gauge length of 10 m and a sampling rate of a 1000 Hz. This resulted in a data volume over 50 TB, which we downsampled to 40 Hz for the analysis in this paper. For this research, we did not have access to an anti-vibration plate. Instead, the interrogator was placed on the concrete floor to minimise vibrations of the interrogator itself. This does affect the data quality, although we can partly mitigate this by filtering the data prior to analysis.

The data shows clear anthropogenic signals from cars on the section on Santorini, and the section near the boundary between the land and sea is always noisy with the primary microseism. The submarine section till approximately 25 km shows clear signals, and the coda from earthquakes lasts much longer there than at any other section of the fibre, see Figure 1c. This is likely due to a sedimentary layer that vanishes after 25 km (Heath et al., 2019). Additionally, the instrumental noise increases with the fibre length, as the optical intensity naturally declines. Figures 1c-e show that small events are measured up to 25 km, while the M6.0 earthquake is visible till 35 km along the fibre. While the data show clear signals from anthropogenic and natural sources, it is challenging to identify distinct arrivals or reflections. The data lacks coherency in space and time, which limits the analysis of the data.

3 Methods

3.1 Event Detection

We detect the local seismicity with an automated image processing algorithm (Thrastarson et al., 2021). The algorithm analyses the entire dataset without requiring manual effort, except for the initial fine-tuning of the parameters and the verification of the results. We verify the results through visualising all detections and manually removing the false positives. The algorithm treats the 2-dimensional data (space & time) as an image and uses image processing to reduce the noise and enhance the features that correspond to local seismicity (Thrastarson et al., 2021). We convert the strain rate data into binary amplitudes with brightness thresholding, which is based on the intensity of the strain rate amplitudes (Otsu, 1979). Regions of True pixels correspond to sections in the data with increased and coherent amplitudes in space and time. Small clusters of True pixels are removed from the data, as well as purely horizontal and vertical patterns affecting single channels, which correspond to instrumental noise. Larger clusters of True regions are retained and classified as seismic events. The algorithm is fully accessible and explained in detail in Thrastarson et al. (2021) and applied in Klaasen et al. (2023).

We adapt the processing steps prior to deploying the algorithm to optimise detections for this specific dataset. First, we only run the detection algorithm on a submarine section of the cable with all channels between 14 and 23 km. This automatically excludes all anthropogenic signals on Santorini and local microseism noise of the coastline, while the data quality of channels beyond 23 km is not sufficient to detect small events. We

process the data by detrending, tapering and applying a bandpass filter between 5 and 19 Hz. The upper boundary is chosen as we run the algorithm on the dataset with a sampling rate of 40 Hz, and the lower boundary is chosen through trial-and-error to optimise detections. The sta-lta algorithm (Allen, 1978) calculates the 2-dimensional characteristic function of the data, which serves to normalise the amplitudes caused by the increasing noise level along the cable. The detection algorithm is then run on this pre-processed data with a moving window of 7.5 s. The size of the moving window allows for separate detections of smaller events that occur with a short time interval in between them. However, the P and S waves of larger, distant events can trigger separate detections. We have manually verified the results, removed false positives and merged separate P and S detections into single events.

The signal-to-noise ratio (SNR) gives a first characterisation of the detected events which can give clues about their origins without requiring accurate locations or magnitudes. We determine the power during the event, and during the 2 s prior to the event with

$$P = \frac{1}{N_t N_c} \sum_{i=0}^{N_t} \sum_{j=0}^{N_c} y_{ij}^2, \tag{1}$$

where N_t is the total number of data points in time, N_c the number of channels, and y_{ij} the amplitude of the sample at time $_i$ and channel $_j$. The ratio between the powers in the time windows before and during the event is taken as the SNR of an event.

To compare the event detections of the DAS fibre with the NOA catalogue, we calculate the theoretical P and S arrival times with IASP91 (Beyreuther et al., 2010; Kennett and Engdahl, 1991) of each earthquake in the NOA catalogue to the fibre. We automatically match detections using the time frame of theoretical arrivals with a broad margin of a few seconds. Then, we manually verify whether the DAS detection is likely to correspond to the event in the NOA catalogue, given its distance and magnitude. With this subset of matched events that have a location and magnitude in the NOA catalogue, we can investigate the detection threshold of the fibre during the acquisition period.

3.2 First-arrival time picking

The first step to locate the events consists of first-arrival time picking, which is challenging for this experiment, due to a lack of "coherency" in the waveforms. We define coherency as a consistency in the polarity of the amplitudes of the waveforms as they are recorded along the fibre. This facilitates the identification of seismic phases in the data. Figure 2b visualises the lack of coherency in the observed data of this experiment. Even though the event has relatively high amplitudes, we can not identify any distinct phase after the onset of the event.

We first attempted to use an automated algorithm that is based on cross-correlations between neighbouring channels with an SNR above a certain threshold, exploiting the coherency of DAS data (Klaasen et al., 2023). This algorithm iteratively refines these relative arrival times by using increasingly small data windows centred around the first arrivals. This methodology worked well for the DAS experiment on Grímsvötn, a subglacial volcano in Iceland where we trenched an optical fibre into the snow (Klaasen et al., 2022, 2023). The fibre was frozen into the snow layer, which resulted in a high data quality. In contrast, the data from this submarine experiment does not show sufficient coherency between channels for an automated picking workflow. Figure 2 compares the data from both experiments, showing coherent waveforms at Grímsvötn, and a lack of coherency for the data in this experiment, even though synthetic simulations would predict coherent waveforms. Both experiments have complex environments, as the submarine fibre likely crosses a subsurface with strong shallow heterogeneities (Capdeville and Sladen, 2024), and the subglacial volcano Grímsvötn has topography, an ice layer, snow and a subglacial lake. Yet at Grímsvötn, the data are more coherent.

In the end, we manually pick the arrival times because (i) there is no clear onset of the events, limiting methods such as the short-term average/long-term average (STA/LTA) algorithm (Withers et al., 1998), (ii) there is no coherence or repetitive pattern in the data, limiting correlation- and template-based approaches, and (iii) the effort of manually picking the arrival times is, for this experiment with only 2 months of data, comparable or less than the effort required to (re-)train a machine learning (ML) algorithm. For DAS experiments with longer temporal durations, we expect that (re-)training ML algorithms would be a sustainable solution for picking. However, existing ML approaches, such as PhaseNet-DAS (Zhu et al., 2023), also depend spatial coherence in the data.

We manually picked the first arrival times by plotting the data and visually selecting a few first arrivals. Consequently, we picked the arrivals times of 5 to 15 channels for each event, depending on the complexity of the waveform. In between the picked arrival times, we linearly interpolated the picks to ensure we have picks along an entire section of the cable. This workflow required a few hours of consistent picking for all events combined.

We only pick one phase for each event, the first *visible* arrivals, as most events do not have multiple arrivals. If multiple arrivals were visible, such as in Figure 1c or 5a, we preferentially picked the P wave. However, for most events we only observe one emergent arrival, such as the events in Figure 1d, 1e or 2b. For those events, we cannot determine with certainty which phase is picked. Most likely, such arrivals correspond to S waves, surface waves or converted waves as they have lower apparent velocities (Daley et al., 2016; Lior et al., 2021). Consequently, we do not have a phase allocation for the events in our catalogue, and the picked seismic phase will vary between events. Unfortunately, the unknown seismic phase of the picked first arrivals will affect the uncertainty of further analysis, such as the event location.

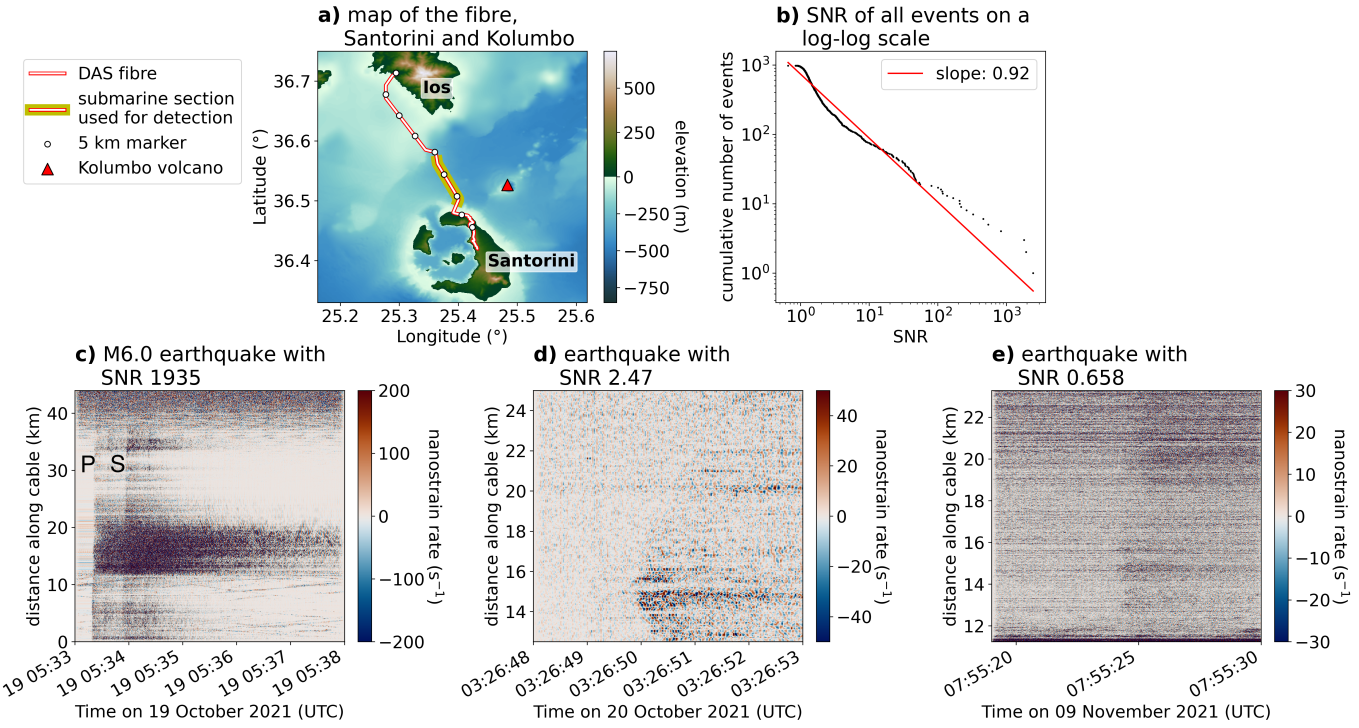

Figure 1 The 45 km long fibre-optic cable extends from Santorini to Ios and can detect events with SNRs varying over four orders of magnitude. a) The fibre connects the two islands following the bathymetry and topography (Ryan et al., 2009), and the highlighted section is the primary section used for event detection and location in this study. b) The SNR distribution of all detected events reveals that the events are likely of natural origin. c) The largest recorded earthquake has a magnitude of 6.0 (National Observatory of Athens, Institute of Geodynamics, 1975). The cable section on Santorini shows signals from cars driving along the roads where the fibre is deployed (diagonal patterns). The earthquake signal continues to resonate at the fibre section between 12 and 21 km due to a layer of sediments characterised by low seismic wave speeds. In general, the SNR drops after 25 km due to the vanishing sedimentary layer and worse cable coupling (Heath et al., 2019; Igel et al., 2024) and keeps decreasing with the fibre length due to the natural decline in optical power. d) Many small events are clearly visible along the highlighted submarine section of the fibre. For such events we can pick first arrival times and locate the event. e) Many quakes are too small and have wavefields too incoherent to pick first arrival times and locate, but we can still detect them even though their amplitudes are comparable to the amplitudes of the ambient noise due to the spatial density of the fibre-optic measurements.

3.3 Event Location

In order to quantify the ability of this DAS experiment to locate events and estimate the location uncertainty, we had to try several location algorithms. First, we attempted to locate the events with the Hamiltonian Monte Carlo algorithm (Zunino et al., 2023), as implemented in Klaasen et al. (2023). While the data fits seemed satisfactory, we noticed a heavy dependence of the final location on the initial random starting position. To have more intuition about this outcome and the fine-tuning parameters, we implemented a simulated annealing algorithm. Again, we noticed sufficient data fits while the dependence on the starting position remained, as well as a trend that all events were located near the submarine section of the fibre. Since this was physically unlikely, we decided to locate the events with a grid search approach, to quantify the event location and uncertainty exactly.

We created a 1-dimensional velocity model from the 3-dimensional heterogeneous velocity model of Heath et al. (2021) as implemented in Igel et al. (2024) by taking the mean velocity of each 200 m layer. We then created a travel time look-up table with this velocity model and the QuakeMigrate package (Hudson et al., 2025). The manually picked and look-up travel times were compared in a grid search over three parameters: longitude, latitude and depth. The misfit between the picked and look-up travel times was given by

$$\chi = \frac{1}{2N} \sum_{i=0}^{N} \frac{\left(t_i^{obs} - t_i^{syn} - t_0\right)^2}{\epsilon^2}, \tag{2}$$

where χ is the misfit, N the number of travel times, t^{obs} the manually picked travel times, t^{syn} the travel times from the look-up table, ϵ the data and model uncertainty, and t_0 the origin time, which is determined by

$$t_0 = \frac{1}{N} \sum_{i=0}^{N} t_i^{obs} - t_i^{syn}. \tag{3}$$

The data and model uncertainty ϵ was determined a posteriori to ensure that the mean normalised misfit converges to 1.

To verify the outcomes, we conducted a synthetic study. We simulated ten different synthetic events with the spectral-element solver Salvus (Afanasiev et al., 2019) and a velocity model that includes topography,

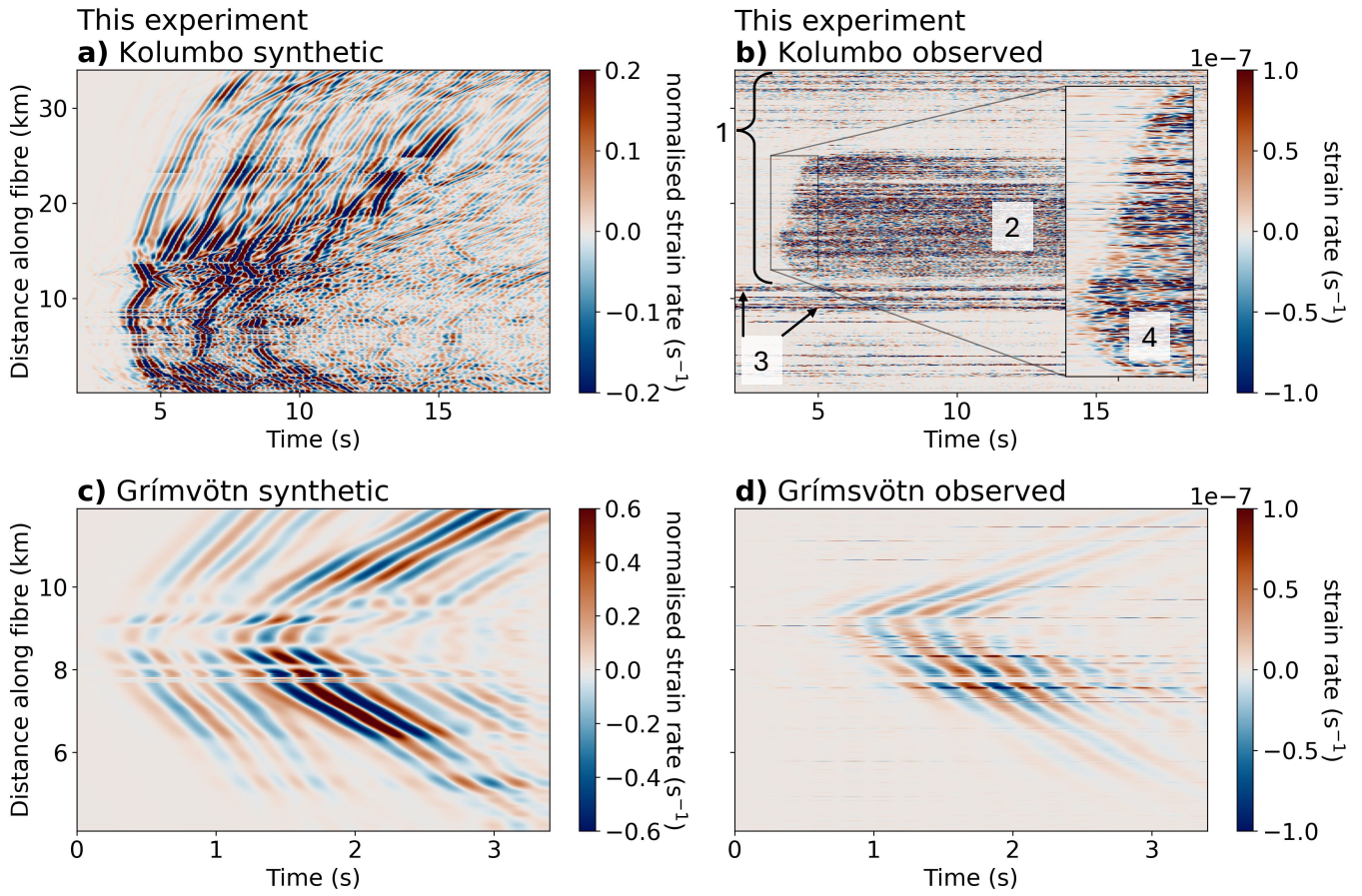

Figure 2 We visualise the "incoherency" in the waveforms of this experiment, in contrast to synthetic data and data from a different DAS experiment that do show seismic arrivals with consistent polarities. The lack of coherent waveforms recorded during this experiment hinders the data analysis. a) We can simulate synthetic data with an earthquake near Kolumbo using a spectral-element solver to model the topography, bathymetry, and heterogeneous subsurface between 0.01 - 3 Hz (Afanasiev et al., 2019; Igel et al., 2024). b) While the synthetic data capture the first arrival of the earthquake, we cannot match any other arrival. The observed data does not show any reflections, refractions or reverberations. There is no coherent waveform along the fibre. **1)** The coupling conditions change along the fibre, as a slow sedimentary layer vanishes beyond 25 km of the fibre (Heath et al., 2019; Igel et al., 2024). Most detected quakes are no longer visible beyond 25 km. **2)** This also affects the complex coda of the earthquakes, as the signal resonates in the section with the slow sedimentary deposits. **3)** The horizontal lines are noisy sections of the fibre near the boundary between the island and sea. **4)** There is no clear onset that is consistent in polarity with distance along the fibre. The polarity of the amplitudes appear randomly, and we cannot identify any individual seismic phase. $t = 0$ corresponds to 2021.10.23 16:49:34 UTC. c) We simulate synthetic data for the DAS experiment at Grímsvötn for a nearby quake with topography, a homogeneous bedrock velocity and the glacier with varying thickness between 1.5 - 3 Hz. d) Due to the coherent polarities at Grímsvötn, we can match the waveforms between the synthetic and observed data. The observed data shows coherent move-outs along the fibre. The coupling conditions of the fibre frozen into the snow are ideal for seismic sensing. $t = 0$ corresponds to 2021.4.14 11:36:57 UTC.

bathymetry, a water layer, and heterogeneous subsurface velocities (Heath et al., 2021). The model setup and simulation details are explained in detail in Igel et al. (2024). The synthetic events were located at different angles and depths with respect to the cable, which were then simulated for our exact fibre layout. We then manually picked the first-arrival times of the synthetic data and located them through the grid search approach to ensure consistency with the process of the observed events.

4 Results & Discussion

The analysis of this experiment initially followed the same methodology as Klaasen et al. (2023). The goal was to detect events with the image-processing algorithm, pick arrival times with an automated workflow, and locate the seismicity with the Hamiltonian Monte Carlo algorithm. However, the data quality and fibre layout of this experiment differ significantly from the Grímsvötn experiment (Klaasen et al., 2023). This forced us to adapt our methodologies, and it revealed some of the challenges that submarine DAS experiments may face.

Figure 2 compares the data quality of both experiments for a local quake. At Grímsvötn, we can simulate synthetic waveforms that match the waveforms of the observed data. For this submarine experiment we can only match the first-arrival times, even though both experiments produced data in complex environments. This emphasises the importance of the cable coupling conditions for telecommunication fibres. At Grímsvötn, the fibre was trenched 50 cm into the snow, resulting in a high data quality. Unfortunately, the exact fibre type, protections of the fibre, fibre location and the installation conditions of the fibre near Santorini are unknown to us. Another possible cause for the lack of onsets that are consistent in polarity with distance along the fibre are shallow subsurface heterogeneities at scales below the earthquake wavelengths (Capdeville and Sladen, 2024). Additionally, we observe most earthquakes only along the first 13 km of the submarine section of the fibre due the data quality, and this section of the fibre is too straight to accurately locate the events.

4.1 Detections

Even though the data lacks coherent waveforms along the fibre, the seismic amplitudes suffice to detect earthquakes. In total, we detect 976 events between 20 October 2021 and 15 December 2021 with the fibre-optic cable. Figure 1 shows the layout of this fibre and a few data examples of the recorded earthquakes. The SNR of the events varies over four orders of magnitude, highlighting the ability of DAS to detect a wide range of events. Figure 1b shows the cumulative distribution of the SNR of each event on a logarithmic plot, with a quasi-b-value for the straight-line fit. This quasi-b-value is comparable to the b-value in a Gutenberg-Richter plot, if all earthquakes were at a similar epicentral distance. We do not observe a clustering of events around some specific SNR values, which hints that the events are predominantly natural in origin, rather than anthropogenic as anthropogenic events tend to repeat with similar energies. The other Figure 1 panels contain different event examples. Panel c shows the largest recorded earthquake, an M6.0 on 19 October 2021, south-east of Crete. Panel d has an example of a small event that the existing catalogue misses and for which we can pick the first-arrival times. Panel e is the detected event with the lowest SNR for which we have no arrival times or location. Due to the spatial density of DAS measurements, we are able to detect events with amplitudes similar to the noise level.

The number of detected events varies over time, as shown in Figure 3, and we observe an anti-correlation between the number of detected events and the wind speed. While the submarine fibre is shielded from the wind directly, the higher wind speeds lead to higher secondary microseism noise levels in the data, which is shown in Igel et al. (2024). Consequently, we detect fewer earthquakes when the wind speed is high, comparable to the on-land seismic stations.

Figure 4a reveals that the subset of events that are detected by DAS and present in the NOA catalogue originate throughout Greece, meaning that the fibre can detect events coming from any azimuth despite its relatively linear layout. We can confirm this by calculating the theoretical sensitivity of the fibre layout to P and S waves coming from any direction, as is visible in Figure S1 in the supplementary information.

4.2 Locations

We pick arrival times for 386 (39%) events, whereas the onsets of the other events were not clear enough to be picked manually. Even manually, the first arrivals of most events were too incoherent to pick with a meaningful level of uncertainty. While this highlights the ability of DAS to detect regional seismicity, it also emphasises the challenge for automating workflows and exploiting the increase in information that DAS offers. The examples in Figure 1 show that the onsets of the different arrivals may be challenging to pick, even though we are able to detect the event. This may be due to the fibre's sensitivity, varying noise levels, source mechanisms, local velocity structure, specific phase conversions or coupling conditions.

An additional challenge of picking the arrival times is the uncertainty in the picked phase. For larger events with multiple arrivals, we can confidently pick the P wave as the first arrival. However, for most events the seismic phase of the arrival times is unknown. Yet, without additional information we have to assume the arrivals correspond to P waves to locate the events, which affects the uncertainty in the resulting event locations.

In the end, we attempt to locate every event using a grid search approach and travel times. The resulting misfits of the events vary, and we normalise them to ensure that the mean value (μ) converges to 1. This normalisation factor corresponds to the total error from the data and theory, ϵ in Equation 2, which is 0.069 s. The distribution of normalised misfits has a standard deviation (σ) of 0.62. The locations have to be interpreted

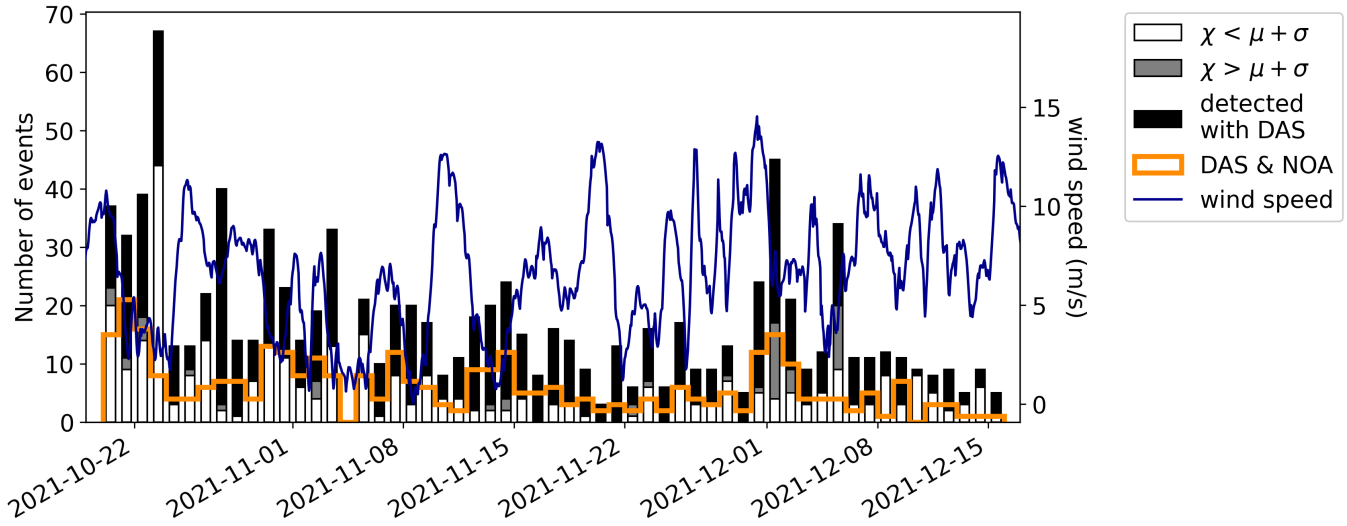

Figure 3 The number of detected events with DAS varies per day. We divide the detected events into three categories: the events that we can locate even though their location is likely inaccurate ($\chi < \mu+\sigma$), the events that we cannot locate with this setup ($\chi > \mu + \sigma$) and the events that are detected but without arrival times ('detected with DAS'). The events that are both detected with DAS and recorded in the NOA catalogue (orange line) correspond mostly to the number of higher quality events, and the average wind speed (Hersbach et al., 2023) (dark blue line) shows an anti-correlation with the recorded events.

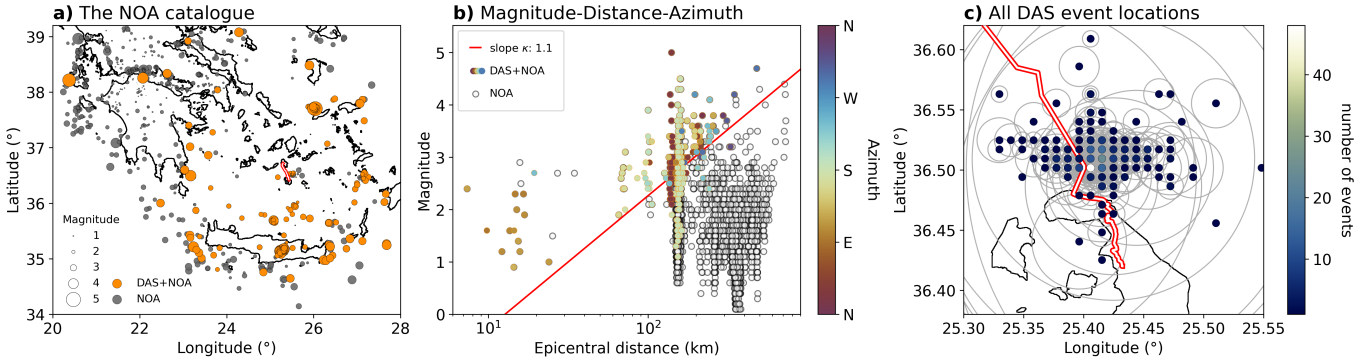

Figure 4 A comparison with the entire catalogue from NOA reveals that DAS can detect events throughout Greece. a) All earthquakes in the NOA catalogue (grey and orange) and the subset of events that are also detected with DAS (orange) are shown with respect to the fibre-optic cable (red-white line) and the Greek islands (black lines). b) The epicentral distance, azimuth and magnitude of the events from panel a with respect to the fibre, as recorded in the NOA catalogue, show which events DAS can detect (coloured) and which events DAS misses (white circle with black edge). The red line symbolises a detection threshold and is manually drawn into the figure. c) 290 events detected with DAS and a misfit below 1.62 ($\chi < \mu+\sigma$) are located in the vicinity of the fibre (red-white line), and their location uncertainty is approximated as a circle (grey).

with care. Firstly, we refrain from interpreting the event locations when the synthetic travel times do not sufficiently fit the observed data with a misfit above 1.62 ($\mu+\sigma$). This may occur when i) the observed data are affected by local velocity structures that are not explained by the 1-dimensional model, ii) the picked arrival times do not correspond to P waves but to different phase arrivals, e.g. surface waves, or iii) the grid search resolution is not high enough as this resolution has been kept low to minimise the computational costs. Secondly, we are *in principle* able to locate the events with misfits below 1.62. However, in this experiment, the submarine section of the fibre is too straight for the events to converge at the correct epicentral location. For example, if we locate an earthquake from Kolumbo using as much of the fibre as possible, we converge at the correct epicentral location, as shown in Figures 5a and c. If we locate the same earthquake using only the submarine section of the fibre as highlighted in Figure 1a, then we do not converge at the correct epicentral location. Figure S2 in the supplementary information shows that the event is then located near the start of the submarine section of the fibre instead of its true epicentral location. Unfortunately, the vast majority of the detected events are only visible along this relatively straight submarine section of the fibre, meaning that our locations are likely inaccurate. Figure 4c shows our locations of the events with a misfit below 1.62, which are all near the start of the submarine fibre section. The grid-like pattern of the locations is due to the gridsearch resolution. The approximate location uncertainty is represented as a circle with a radius equal to that of the surface containing the horizontal 2-dimensional misfit volume that is calculated with one error deviation (ϵ) of 0.069 s.

We conduct synthetic tests to verify our ability to locate events. Figure S3 in the supplementary information shows that we approximate the correct epicentral location when we use the entire fibre, but not the correct depth. For a correct depth resolution, we would need both P and S wave picks or a larger vertical profile of the fibre. Picking both P and S waves is often impossible for the many small events that DAS detects that are underneath the detection threshold of existing networks, such as the event in Figure 1d. In order to refine the resolved epicentral location of an event, we add a second hypothetical fibre, connecting the island of Santorini with Anafi. Figure S4 shows that using multiple fibres with different azimuthal directions improves the event location and lowers the uncertainty. If a pre-existing fibre is too linear for event location, a network of fibres can be interrogated to increase the azimuthal coverage.

4.3 Comparison with the existing catalogue

In order to compare the performance of DAS with the existing network from NOA, we consider the number of events that are detected and their locations. Figure 3 reveals the number of detected events per day with DAS, subdivided into three categories that correspond to the quality of the event; events that are located with a misfit below the mean and one standard deviation ($\chi < \mu+\sigma$), events that have manually picked arrival times but cannot be located ($\chi > \mu + \sigma$) and events that are detected but have no arrival times ('detected with DAS'). In total, 243 events are recorded both by DAS and in the NOA catalogue (orange line), which largely correspond to the higher quality events detected with DAS. Both the earthquake detections recorded in the NOA and DAS catalogues show an anti-correlation with the wind speed, as few earthquakes are detected during periods with higher wind speeds.

Figure 4 compares the earthquake locations from the NOA catalogue and the DAS experiment. Panel a shows all earthquakes in the NOA catalogue during this experiment's acquisition period, and the subset of events that are both recorded with DAS and in the NOA catalogue. DAS is able to detect events throughout Greece, which means that it is sensitive to events coming from any direction despite its relatively straight layout and single-component measurements. Panel b shows the epicentral distance, magnitude and azimuth of the earthquakes from panel a with respect to the fibre, as recorded in the NOA catalogue. For this subset of events, we can investigate the detection threshold of the DAS experiment through a general relationship between the magnitude M and the epicentral distance R (Aki and Richards, 2002),

$$M = \log_{10}(A) + \kappa \log_{10}(R) + C, \tag{4}$$

where A is the recorded amplitude and C a constant. If we rearrange the equation and assume the minimum recorded amplitude of A_o, the detection threshold is influenced by

$$M - \kappa \log_{10}(R) > \log_{10}(A_o) + C, \tag{5}$$

where the constant κ links the detected magnitude with the distance. We can manually draw a straight line through Figure 4b to determine the value of κ, which symbolises the detection threshold of the fibre compared to the distance and magnitude of these earthquakes. There are outliers on each side of the line. There are two distinct clusters of seismic activity oriented favourably relative to the fibre, north of Ikaria and beneath Crete, that cross the line where DAS detects events down to smaller magnitudes relative to their distance.

A direct comparison of the ability of the networks to locate one earthquake from Kolumbo reveals that the Greek network outperforms the DAS experiment for location accuracy and uncertainty. For this comparison, we retrieve the arrival times from the national network for the stations shown in Figure 5d and we repeat the process of event locations for the DAS channels (Figure 5c), the Greek stations (Figure 5d), and both simultaneously (Figure 5b). The epicentral location is most accurate and has the lowest uncertainty when we only consider the Greek seismic stations. The joint inversion improves upon the results compared to the inversion using only the fibre-optic cable. However, it is dominated by the DAS channels as each station has a similar weight during the inversion. A careful weighing scheme would

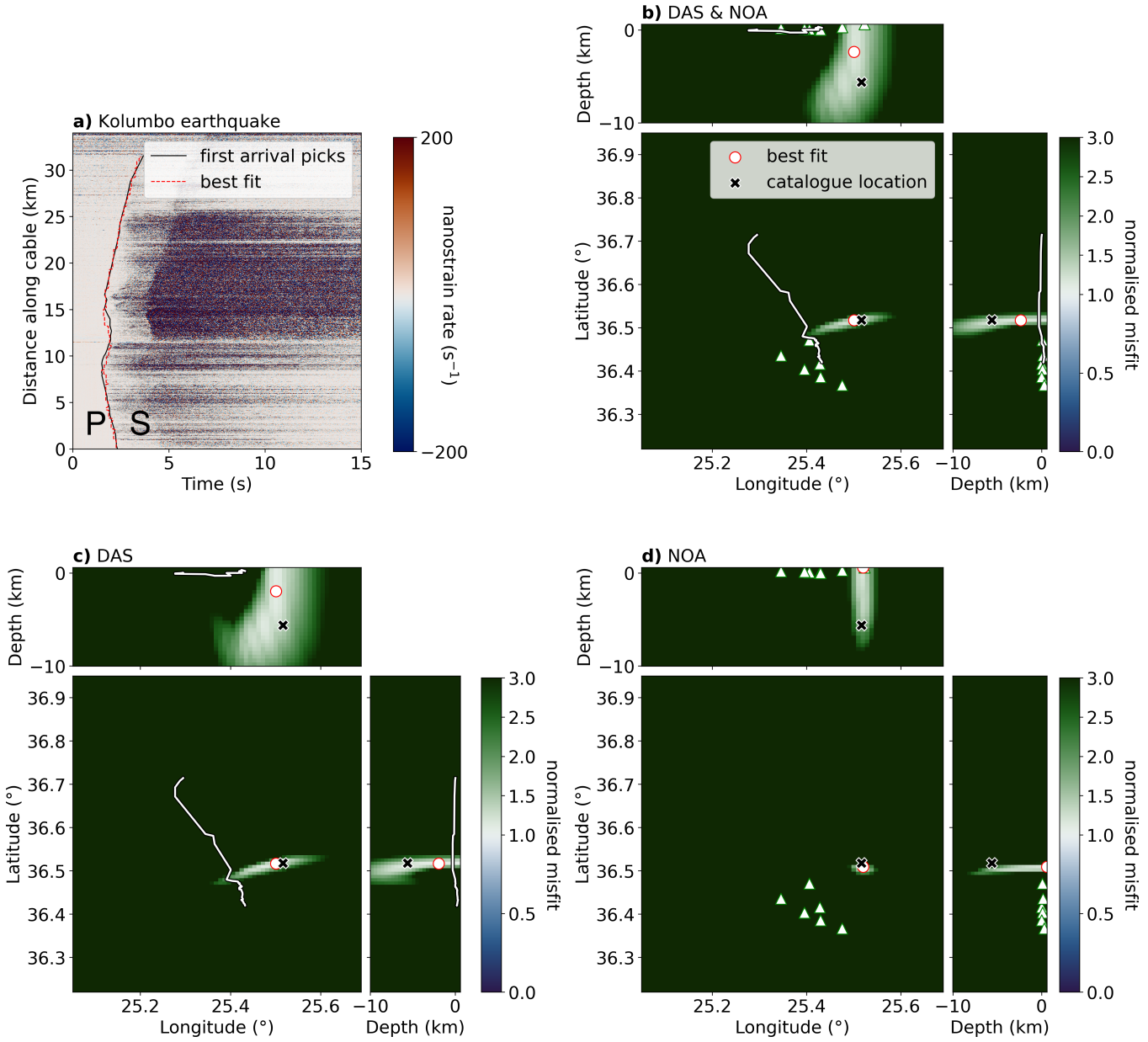

Figure 5 The comparison between event locations with DAS and the NOA catalogue reveals that a wider spatial coverage is more important for accurate locations than spatially dense stations. a) An earthquake from Kolumbo is recorded both by the fibre and the seismic stations on Santorini. The manually picked arrival times (black line) are matched with synthetic travel times (the red dashed line gives the synthetic travel times from the location with the lowest misfit). b) The result using both DAS channels and seismic stations shows an accurate epicentral location with a slightly smaller location uncertainty compared to the result in c, which uses only the DAS channels. c) The inversion using as many DAS channels as possible converges at the correct epicentral location. If we use fewer channels for this inversion, e.g. only the submarine section, then the event is located incorrectly, near the start of the submarine section of the fibre. d) The lowest location uncertainty is achieved when only the seismic stations on Santorini are used in the inversion. For a correct depth resolution, we require S wave picks or a larger vertical profile of the networks.

be necessary to ensure that the larger coverage of sparse networks is not lost in the inversion.

5 Conclusions

Fibre-optic networks have the potential to augment existing seismic monitoring networks for targeted earthquake and volcano monitoring on a local scale. The enhanced spatial density leads to a lower detection threshold and significant information gain in areas that may otherwise remain inaccessible for real-time monitoring, such as the submarine environment. However, the earthquake detections in the submarine environment are also limited by the wind-driven oceanic wave noise. Higher wind speeds lead to higher levels of secondary microseism noise, which can obscure smaller events.

At the same time, submarine DAS experiments may face challenges. The largest challenges we identify for DAS experiments with telecommunication fibres are the unknown cable coupling conditions that may lower the data quality, shallow subsurface effects that perturb the strain wavefield, and the fibre layout. The data quality might not suffice for automated workflows, which limits the potential of DAS for real-time monitoring. This research required significant manual input to pick the first arrival times of the earthquakes. Even manually, the first arrivals of the majority of the events were not distinct enough to pick. In order to accurately locate seismicity, the fibre needs to have a sufficient azimuthal coverage. However, the exact conditions of telecommunication fibres are generally outside the control of the researcher.

The joint operation of fibre-optic networks with seismic stations would increase the azimuthal coverage and lead to more accurate event locations, as long as the different measurements are carefully integrated into joint inversions. For small-scale monitoring, a single fibre-optic array may suffice if its layout is specifically designed with the target area in mind. For Kolumbo, a network of existing fibre-optic cables that connects the surrounding islands may potentially lead to a real-time and high-resolution submarine monitoring network that can detect and locate small volcano-tectonic events.

6 Acknowledgements

The authors gratefully acknowledge all the support we received from OTE, who provided us with access to the fibre-optic cable and support in the field.

7 Additional Information

The event detection algorithm is available at https://github.com/solvithrastar/DAS_Auto. A Jupyter notebook that shows the manual travel time picking with the Kolumbo earthquake from Figure 5 is available at https://github.com/saraklaasen/manual_picking_DAS. The QuakeMigrate package, used to create travel time look-up tables and the sensitivity plots in Figure S1, is available at https://github.com/QuakeMigrate/QuakeMigrate. All figures are created with scientific colour maps (Crameri, 2018). The earthquake catalogue that we, for simplicity, refer to as "the NOA catalogue" was retrieved from http://www.geophysics.geol.uoa.gr/stations/gmapv3_db/index.php?lang=en on 22 January 2024. The data from the stations in Figure 5 are part of the seismic networks HL, HT and HA (National Observatory of Athens, Institute of Geodynamics, 1975; Aristotle University of Thessaloniki, 1981; University of Athens, 2008).

8 Data Availability

The earthquake catalogue created during this study is available in the supplementary information. The complete DAS dataset is over 50 TB and stored on tape at ETH Zürich. The decimated dataset is still 7.7 TB, which can be shared upon request.

9 Ethical Statement

This research did not require approval from an ethics committee.

10 Competing Interests

The authors declare no competing interests.

11 Funding Declaration

This research was fully funded by ETH Zürich.

References

Afanasiev, M., Boehm, C., van Driel, M., Krischer, L., Rietmann, M., May, D. A., Knepley, M. G., and Fichtner, A. Modular and flexible spectral-element waveform modelling in two and three dimensions. *Geophysical Journal International*, 216(3):1675–1692, 2019. doi: 10.1093/gji/ggy469.

Aki, K. and Richards, P. G. *Quantitative seismology*. 2002.

Allen, R. V. Automatic earthquake recognition and timing from single traces. *Bulletin of the seismological society of America*, 68(5): 1521–1532, 1978. doi: 10.1785/BSSA0680051521.

Aristotle University of Thessaloniki. Aristotle University of Thessaloniki Seismological Network, 1981. doi: 10.7914/SN/HT.

Azzola, J., Thiemann, K., and Gaucher, E. Integration of distributed acoustic sensing for real-time seismic monitoring of a geothermal field. *Geothermal Energy*, 11(1):30, 2023. doi: 10.1186/s40517-023-00272-4.

Beyreuther, M., Barsch, R., Krischer, L., Megies, T., Behr, Y., and Wassermann, J. ObsPy: A Python toolbox for seismology. *Seismological Research Letters*, 81(3):530–533, 2010. doi: 10.1785/gssrl.81.3.530.

Biagioli, F., Métaxian, J.-P., Stutzmann, E., Ripepe, M., Bernard, P., Trabattoni, A., Longo, R., and Bouin, M.-P. Array analysis of seismo-volcanic activity with distributed acoustic sensing. *Geophysical Journal International*, 236(1):607–620, 2024.

Brüstle, A., Friederich, W., Meier, T., and Gross, C. Focal mechanism and depth of the 1956 Amorgos twin earthquakes from waveform matching of analogue seismograms. *Solid Earth*, 5 (2):1027–1044, 2014. doi: 10.5194/se-5-1027-2014.

Cantner, K., Carey, S., and Nomikou, P. Integrated volcanologic and petrologic analysis of the 1650 AD eruption of Kolumbo submarine volcano, Greece. *Journal of Volcanology and Geothermal Research*, 269:28–43, 2014. doi: 10.1016/j.jvolgeores.2013.10.004.

Capdeville, Y. and Sladen, A. DAS sensitivity to heterogeneity scales much smaller than the minimum wavelength. *Seismica*, 3(1), 2024. doi: 10.26443/seismica.v3i1.1007.

Cheng, F., Chi, B., Lindsey, N. J., Dawe, T. C., and Ajo-Franklin, J. B. Utilizing distributed acoustic sensing and ocean bottom fiber optic cables for submarine structural characterization. *Scientific reports*, 11(1):5613, 2021. doi: 10.1038/s41598-021-84845-y.

Cheng, F., Ajo-Franklin, J. B., Nayak, A., Tribaldos, V. R., Mellors, R., Dobson, P., and Team, I. V. D. F. Using dark fiber and distributed acoustic sensing to characterize a geothermal system in the Imperial Valley, Southern California. *Journal of Geophysical Research: Solid Earth*, 128(3):e2022JB025240, 2023. doi: 10.1029/2022JB025240.

Crameri, F. Scientific colour maps. *Zenodo*, 10:5281, 2018. doi: 10.5281/zenodo.1243862.

Currenti, G., Jousset, P., Napoli, R., Krawczyk, C., and Weber, M. On the comparison of strain measurements from fibre optics with a dense seismometer array at Etna volcano (Italy). *Solid Earth*, 12(4):993–1003, 2021. doi: 10.5194/se-12-993-2021.

Daley, T. M., Miller, D. E., Dodds, K., Cook, P., and Freifeld, B. M. Field testing of modular borehole monitoring with simultaneous distributed acoustic sensing and geophone vertical seismic profiles at Citronelle, Alabama. *Geophys. Prosp.*, 64:1318–1334, 2016. doi: 10.1111/1365-2478.12324.

Evangelidis, C. and Melis, N. Ambient noise levels in Greece as recorded at the Hellenic Unified Seismic Network. *Bulletin of the Seismological Society of America*, 102(6):2507–2517, 2012. doi: 10.1785/0120110319.

Gou, Y., Allen, R. M., Zhu, W., Taira, T., and Chen, L. Leveraging Submarine DAS Arrays for Offshore Earthquake Early Warning: A Case Study in Monterey Bay, California. *Bulletin of the Seismological Society of America*, Jan. 2025. doi: 10.1785/0120240234.

Grandi, S., Dean, M., and Tucker, O. Efficient containment monitoring with distributed acoustic sensing: feasibility studies for the former Peterhead CCS Project. *Energy Procedia*, 114:3889–3904, 2017. doi: 10.1016/j.egypro.2017.03.1521.

Hartog, A. H. *An introduction to distributed optical fibre sensors*. CRC press, 2017. doi: 10.1201/9781315119014.

Heath, B., Hooft, E., Toomey, D., Papazachos, C., Nomikou, P., Paulatto, M., Morgan, J., and Warner, M. Tectonism and its relation to magmatism around Santorini Volcano from upper crustal P wave velocity. *Journal of Geophysical Research: Solid Earth*, 124(10):10610–10629, 2019. doi: 10.1029/2019JB017699.

Heath, B., Hooft, E., Toomey, D., Paulatto, M., Papazachos, C., Nomikou, P., and Morgan, J. Relationship between active faulting/fracturing and magmatism around Santorini: Seismic anisotropy from an active source tomography experiment. *Journal of Geophysical Research: Solid Earth*, 126(8): e2021JB021898, 2021. doi: 10.1029/2021JB021898.

Hersbach, H., Bell, B., Berrisford, P., Biavati, G., Horányi, A., Muñoz Sabater, J., Nicolas, J., Peubey, C., Radu, R., Rozum, I., Schepers, D., Simmons, A., Soci, C., Dee, D., and Thépaut, J.-N. ERA5 hourly data on single levels from 1940 to present. *Copernicus Climate Change Service (C3S) Climate Data Store (CDS)*, 2023. doi: 10.24381/cds.adbb2d47.

Hudson, T. S., Klaasen, S., Fontaine, O., Bacon, C., Jonsdottir, K., and Fichtner, A. Towards a widely applicable earthquake detection algorithm for fibreoptic and hybrid fibreoptic-seismometer networks. *Geophysical Journal International*, 240(3):1965–1985, 02 2025. doi: 10.1093/gji/ggae459.

Igel, J. K., Klaasen, S., Noe, S., Nomikou, P., Karantzalos, K., and Fichtner, A. Challenges in submarine fiber-optic earthquake monitoring. *Journal of Geophysical Research: Solid Earth*, 129 (12):e2024JB029556, 2024. doi: 10.1029/2024JB029556.

(ITSAK) Institute of Engineering Seimology Earthquake Engineering. ITSAK Strong Motion Network, 1981. doi: 10.7914/SN/HI.

Joe, H.-E., Zhou, F., Yun, S.-T., and Jun, M. B. Detection and quantification of underground CO2 leakage into the soil using a fiber-optic sensor. *Optical Fiber Technology*, 60:102375, 2020. doi: 10.1016/j.yofte.2020.102375.

Jousset, P., Reinsch, T., Ryberg, T., Blanck, H., Clarke, A., Aghayev, R., Hersir, G. P., Henninges, J., Weber, M., and Krawczyk, C. M. Dynamic strain determination using fibre-optic cables allows imaging of seismological and structural features. *Nature communications*, 9(1):1–11, 2018. doi: 10.1038/s41467-018-04860-y.

Jousset, P., Currenti, G., Schwarz, B., Chalari, A., Tilmann, F., Reinsch, T., Zuccarello, L., Privitera, E., and Krawczyk, C. M. Fibre optic distributed acoustic sensing of volcanic events. *Nature communications*, 13(1):1–16, 2022. doi: 10.1038/s41467-022-29184-w.

Kennett, B. and Engdahl, E. Traveltimes for global earthquake location and phase identification. *Geophysical Journal International*, 105(2):429–465, 1991. doi: 10.1111/j.1365-246X.1991.tb06724.x.

Klaasen, S., Noe, S., Thrastarson, S., Çubuk-Sabuncu, Y., , Jónsdóttir, K., and Fichtner, A. Strategies for source inversion with full-waveform modelling and distributed acoustic sensing on a subglacial volcano. Unpublished, in prep.

Klaasen, S., Paitz, P., Lindner, N., Dettmer, J., and Fichtner, A. Distributed acoustic sensing in volcano-glacial environments—Mount Meager, British Columbia. *Journal of Geophysical Research: Solid Earth*, 126(11), 2021. doi: 10.1029/2021JB022358.

Klaasen, S., Thrastarson, S., Fichtner, A., Cubuk-Sabuncu, Y., and Jónsdóttir, K. Sensing Iceland's Most Active Volcano with a "Buried Hair". *Eos*, 103, 2022. doi: 10.1029/2022EO220007.

Klaasen, S., Thrastarson, S., Çubuk-Sabuncu, Y., Jónsdóttir, K., Gebraad, L., Paitz, P., and Fichtner, A. Subglacial volcano monitoring with fibre-optic sensing: Grímsvötn, Iceland. *Volcanica*, 6(2): 301–311, 2023. doi: 10.30909/vol.06.02.301311.

Lellouch, A., Lindsey, N. J., Ellsworth, W. L., and Biondi, B. L. Comparison between distributed acoustic sensing and geophones: Downhole microseismic monitoring of the FORGE geothermal experiment. *Bulletin of the Seismological Society of America*, 91 (6):3256–3268, 2020. doi: 10.1785/0220200149.

Li, J., Zhu, W., Biondi, E., and Zhan, Z. Earthquake focal mechanisms with distributed acoustic sensing. *Nature Communications*, 14(1):4181, 2023. doi: 10.1038/s41467-023-39639-3.

Li, Z. and Zhan, Z. Pushing the limit of earthquake detection with distributed acoustic sensing and template matching: A case study at the Brady geothermal field. *Geophysical Journal International*, 215(3):1583–1593, 2018. doi: 10.1093/gji/ggy359.

Lindsey, N. J. and Martin, E. R. Fiber-optic seismology. *Annual Review of Earth and Planetary Sciences*, 49:309–336, 2021. doi: 10.1146/annurev-earth-072420-065213.

Lior, I., Sladen, A., Rivet, D., Ampuero, J.-P., Hello, Y., Becerril, C., Martins, H. F., Lamare, P., Jestin, C., Tsagkli, S., and Markou, C. On the detection capabilities of underwater distributed acoustic sensing. *Journal of Geophysical Research: Solid Earth*, 126(3): e2020JB020925, 2021. doi: 10.1029/2020JB020925.

Martuganova, E., Stiller, M., Norden, B., Henninges, J., and Krawczyk, C. M. 3D deep geothermal reservoir imaging with

wireline distributed acoustic sensing in two boreholes. *Solid Earth*, 13(8):1291–1307, 2022. doi: 10.5194/se-13-1291-2022.

Mateeva, A., Lopez, J., Potters, H., Mestayer, J., Cox, B., Kiyashchenko, D., Wills, P., Grandi, S., Hornman, K., Kuvshinov, B., Berlang, W., Yang, Z., and Detomo, R. Distributed acoustic sensing for reservoir monitoring with vertical seismic profiling. *Geophysical Prospecting*, 62(4):679–692, 2014. doi: 10.1111/1365-2478.12116.

National Observatory of Athens, Institute of Geodynamics. National observatory of Athens seismic network [Dataset]. *International Federation of Digital Seismograph Networks*, 1975. doi: 10.7914/SN/HL.

Nayak, A., Ajo-Franklin, J., and the Imperial Valley Dark Fiber Team. Distributed acoustic sensing using dark fiber for array detection of regional earthquakes. *Seismological Research Letters*, 92(4): 2441–2452, 2021. doi: 10.1785/0220200416.

Nishimura, T., Emoto, K., Nakahara, H., Miura, S., Yamamoto, M., Sugimura, S., Ishikawa, A., and Kimura, T. Source location of volcanic earthquakes and subsurface characterization using fiber-optic cable and distributed acoustic sensing system. *Scientific reports*, 11(1):6319, 2021. doi: 10.1038/s41598-021-85621-8.

Nomikou, P., Hübscher, C., and Carey, S. The Christiana–Santorini–Kolumbo volcanic field. *Elements: An International Magazine of Mineralogy, Geochemistry, and Petrology*, 15(3): 171–176, 2019. doi: 10.2138/gselements.15.3.171.

Okal, E. A., Synolakis, C. E., Uslu, B., Kalligeris, N., and Voukouvalas, E. The 1956 earthquake and tsunami in Amorgos, Greece. *Geophysical Journal International*, 178(3):1533–1554, 2009. doi: 10.1111/j.1365-246X.2009.04237.x.

Otsu, N. A threshold selection method from gray-level histograms. *IEEE transactions on systems, man, and cybernetics*, 9(1):62–66, 1979.

Ouellet, S. M., Dettmer, J., Lato, M. J., Cole, S., Hutchinson, D. J., Karrenbach, M., Dashwood, B., Chambers, J. E., and Crickmore, R. Previously hidden landslide processes revealed using distributed acoustic sensing with nanostrain-rate sensitivity. *Nature Communications*, 15(1):6239, 2024. doi: 10.1038/s41467-024-50604-6.

Paitz, P., Edme, P., Gräff, D., Walter, F., Doetsch, J., Chalari, A., Schmelzbach, C., and Fichtner, A. Empirical investigations of the instrument response for distributed acoustic sensing (DAS) across 17 octaves. *Bulletin of the Seismological Society of America*, 111(1):1–10, 2021. doi: 10.1785/0120200185.

Pevzner, R., Isaenkov, R., Yavuz, S., Yurikov, A., Tertyshnikov, K., Shashkin, P., Gurevich, B., Correa, J., Glubokovskikh, S., Wood, T., Freifeld, B., and Barraclough, P. Seismic monitoring of a small CO2 injection using a multi-well DAS array: Operations and initial results of Stage 3 of the CO2CRC Otway project. *International Journal of Greenhouse Gas Control*, 110:103437, 2021. doi: 10.1016/j.ijggc.2021.103437.

Ryan, W. B., Carbotte, S. M., Coplan, J. O., O'Hara, S., Melkonian, A., Arko, R., Weissel, R. A., Ferrini, V., Goodwillie, A., Nitsche, F., Bonczkowksi, J., and Zemsky, R. Global multi-resolution topography synthesis. *Geochemistry, Geophysics, Geosystems*, 10(3), 2009. doi: 10.1029/2008GC002332.

Spica, Z. J., Nishida, K., Akuhara, T., Pétrélis, F., Shinohara, M., and Yamada, T. Marine sediment characterized by ocean-bottom fiber-optic seismology. *Geophysical Research Letters*, 47(16): e2020GL088360, 2020. doi: 10.1029/2020GL088360.

Technological Educational Institute of Crete. Seismological Network of Crete, 2006. doi: 10.7914/SN/HC.

Thrastarson, S., Torfason, R., Klaasen, S., Paitz, P., Cubuk-Sabuncu, Y., Jónsdóttir, K., and Fichtner, A. Detecting Seismic Events with Computer Vision: Applications for Fiber-Optic Sensing. *ESS Open Archive*, 2021. doi: 10.1002/essoar.10509693.1.

Trafford, A., Ellwood, R., Wacquier, L., Godfrey, A., Minto, C., Coughlan, M., and Donohue, S. Distributed acoustic sensing for active offshore shear wave profiling. *Scientific Reports*, 12(1):9691, 2022. doi: 10.1038/s41598-022-13962-z.

Tuinstra, K., Grigoli, F., Lanza, F., Rinaldi, A. P., Fichtner, A., and Wiemer, S. Locating clustered seismicity using Distance Geometry Solvers: applications for sparse and single-borehole DAS networks. *Geophysical Journal International*, 238(2):661–680, 2024. doi: 10.1093/gji/ggae168.

Ulvrova, M., Paris, R., Nomikou, P., Kelfoun, K., Leibrandt, S., Tappin, D., and McCoy, F. Source of the tsunami generated by the 1650 AD eruption of Kolumbo submarine volcano (Aegean Sea, Greece). *Journal of Volcanology and Geothermal Research*, 321: 125–139, 2016. doi: 10.1016/j.jvolgeores.2016.04.034.

University of Athens. Hellenic Seismological Network, University of Athens, Seismological Laboratory, 2008. doi: 10.7914/SN/HA.

Wang, H. F., Zeng, X., Miller, D. E., Fratta, D., Feigl, K. L., Thurber, C. H., and Mellors, R. J. Ground motion response to an ML 4.3 earthquake using co-located distributed acoustic sensing and seismometer arrays. *Geophysical Journal International*, 213(3): 2020–2036, 2018. doi: 10.1093/gji/ggy102.

Williams, E. F., Fernández-Ruiz, M. R., Magalhaes, R., Vanthillo, R., Zhan, Z., González-Herráez, M., and Martins, H. F. Distributed sensing of microseisms and teleseisms with submarine dark fibers. *Nature communications*, 10(1):5778, 2019. doi: 10.1038/s41467-019-13262-7.

Withers, M., Aster, R., Young, C., Beiriger, J., Harris, M., Moore, S., and Trujillo, J. A comparison of select trigger algorithms for automated global seismic phase and event detection. *Bulletin of the Seismological Society of America*, 88(1):95–106, 1998. doi: 10.1785/BSSA0880010095.

Xie, T., Zhang, C.-C., Shi, B., Chen, Z., and Zhang, Y. Integrating distributed acoustic sensing and computer vision for real-time seismic location of landslides and rockfalls along linear infrastructure. *Landslides*, pages 1–19, 2024. doi: 10.1007/s10346-024-02268-y.

Zhu, W., Biondi, E., Li, J., Yin, J., Ross, Z. E., and Zhan, Z. Seismic arrival-time picking on distributed acoustic sensing data using semi-supervised learning. *Nature Communications*, 14(1):8192, 2023. doi: 10.1038/s41467-023-43355-3.

Zunino, A., Gebraad, L., Ghirotto, A., and Fichtner, A. HMCLab: a framework for solving diverse geophysical inverse problems using the Hamiltonian Monte Carlo method. *Geophysical Journal International*, 235(3):2979–2991, 2023. doi: 10.1093/gji/ggad403.